

Article

Parameters for the Formation of the Dobroe Gold Deposit (Yenisei Ridge, Russia): Evidence from Fluid Inclusions and S–C Isotopes

Elena Shaparenko ^{1,*}, Nadezhda Gibsher ¹, Margarita Khomenko ¹, Anatoly Tomilenko ¹, Anatoly Sazonov ², Taras Bul'bak ¹, Sergey Silyanov ², Marina Petrova ¹ and Maria Ryabukha ¹

¹ Sobolev Institute of Geology and Mineralogy, Siberian Branch of the Russian Academy of Sciences, 630090 Novosibirsk, Russia

² Department of Geology, Mineralogy and Petrography, Siberian Federal University, 660041 Krasnoyarsk, Russia

* Correspondence: shaparenko@igm.ncs.ru

Abstract: The Dobroe deposit with 10 t gold reserves is one of the gold mines located within the Yenisei Ridge Orogenic Belt. The ore-forming conditions of orogenic gold deposits are have recently been widely discussed. A comprehensive study of fluid inclusions revealed that the Dobroe gold deposit was formed by water–carbon dioxide and carbon dioxide–hydrocarbon fluids within a temperature range of 180 to 360 °C, a pressure range of 0.8 to 1.3 kbar, and a salinity range of 1.5 to 15.0 wt.% (NaCl-equiv.). Gas chromatography–mass spectrometry showed that ore-forming fluids consisted of H₂O, CO₂, hydrocarbons, nitrogenated, sulfonated, and chlorinated compounds. The distribution patterns of $\delta^{13}\text{C}$ in fluid inclusions (−11.3‰–−3.6‰) and $\delta^{34}\text{S}$ in sulfides (1.9‰–17‰) of the Dobroe deposit indicate a crustal source for ore-bearing fluids.

Keywords: orogenic gold deposits; Yenisei Ridge; fluid inclusions; gas chromatography–mass spectrometry



Citation: Shaparenko, E.; Gibsher, N.; Khomenko, M.; Tomilenko, A.; Sazonov, A.; Bul'bak, T.; Silyanov, S.; Petrova, M.; Ryabukha, M. Parameters for the Formation of the Dobroe Gold Deposit (Yenisei Ridge, Russia): Evidence from Fluid Inclusions and S–C Isotopes. *Minerals* **2023**, *13*, 11. <https://doi.org/10.3390/min13010011>

Academic Editor: Nuo Li

Received: 9 November 2022

Revised: 7 December 2022

Accepted: 19 December 2022

Published: 22 December 2022



Copyright: © 2022 by the authors. Licensee MDPI, Basel, Switzerland. This article is an open access article distributed under the terms and conditions of the Creative Commons Attribution (CC BY) license (<https://creativecommons.org/licenses/by/4.0/>).

1. Introduction

At present, primary deposits are the main source of gold. The Yenisei Ridge is a strategically important region of Russia with regard to gold mining [1]. The gold ore deposits in the Yenisei Ridge are of the orogenic type [2]. There are likely more than 3000 t in reserves of ore fold [3,4]. Within the gold-bearing orogenic belt, deposits with predicted gold resources of more than 100 t are known of and are being mined, including Olimpiada, Blagodatnoye, and Sovetskoe [4–6]. The deposits are located in shear zones and confined to fault zones. The ore bodies are represented by gold-sulfide quartz veins in the host metamorphic strata [7]. More than 100 primary gold ore occurrences with predicted resources of less than 10 t have also been identified on the Yenisei Ridge [4,8,9].

The Dobroe gold deposit, which has a predicted gold resource of about 10 t, is located 12 km from the Sovetskoe deposit, where over 100 t of gold has already been mined [4].

A huge number of factors affect the scale of a gold deposit [10]. There are several points of view regarding the genetic reasons for the localization of gold mineralization in deposits of different scales in terms of Au reserves. Some researchers [11,12] assume that the primary gold enrichment of ore-bearing rocks is associated with submarine hydrothermal activity near the junctions between basement faults, which are repeatedly melted and control the placement of gold-bearing hydrothermal mineralization. Other researchers [7,13–26] believe that the deposits are formed as a result of hydrothermal solutions rising from the deep horizons of the Earth's crust. In hydrothermal models, ore-forming fluids of the Yenisei gold deposits play a major role in gold ore genesis [19–30]. In recent years, a new genetic model for the formation of gold-sulfide mineralization associated with mantle plume magmatism has been proposed within the tectonic evolution of the Yenisei Ridge [31,32].

Despite the variety of traditional fluid inclusion and isotope studies that have been conducted, the genesis of orogenic gold deposits still remains a debated topic [33–35]. Currently, there are two variations of the most viable metamorphic model: the slab devolatilization hypothesis, and the devolatilization of deeper supracrustal sequences underlying the host rocks of the deposit [33].

Improvement on the traditional thermobarogeochemical and the involvement of new methods and the latest generation of instruments [26,36] has allowed researchers to reveal the physicochemical parameters of the fluids involved in the formation of different scale gold deposits. These fluid properties can be used for clarifying the model of orogenic gold deposit formation, as well as for practical purposes in the ongoing search for, exploration, and evaluation of new gold occurrences.

The aim of this study was to reveal the ore-forming conditions of quartz-sulfide veins from the Dobroe gold deposit.

2. Geology and Mineralogy of the Deposit

The Dobroe deposit is a part of the Sovetsky ore cluster and is located 12 km west of the Sovetsky deposit, one of the largest in the Yenisei Ridge (Figure 1). The deposit was discovered during a geological survey carried out between 1976 and 1980. Gold mining at the deposit has been carried out via open-pit mining since 1992. Ores from the Dobroe deposit are processed at the Sovetskaya gold processing plant.

The Sovetsky ore cluster is confined to the junction zone of two large Proterozoic structures of the Yenisei Ridge: the Central Uplift and the eastern synclinal zone [37]. The boundary between the two structures is the Ishimba deep fault, which dictates the location of most gold-quartz deposits, including the Sovetskoe, Aleksandro-Ageevskoe, Polyarnaya Zvezda, Zayavka 14, Eldorado, and Dobroe deposits [7,38,39].

The major structure of the ore field is the Sergievskaya syncline, composed of deposits of the Corda and Gorbiloksk formations, metamorphosed under the conditions of the greenschist facies of regional metamorphism. Faults are established within the ore field, which are distinguished by zones of crushing and mylonitization with a thickness of 1–2 or 10–30 m. Ore bodies are concentrated in these zones, represented by hydrothermally altered schists containing quartz veins and veinlets with gold-sulfide mineralization.

The outcrops of granitoids from the Tatar-Ayakhta complex (RF₃ta) on the present surface are located 5 km southwest of the Dobroe deposit.

The deposit is in a separate tectonic block; bounded in the southwest by the West Ishimba deep fault, in the northeast by the Serafimovsky fault, and in the northwest and southeast, it is limited by sublatitudinal faults.

The deposit is a lenticular-shaped quartz-vein zone with a length of up to 2700 m, a thickness of up to 27.5 m, and a vertical span of mineralization of up to 540 m [7]. The ore bodies comprise thin quartz veins, lenses, vein zones, and metasomatically altered host quartz-sericite-chlorite schists, which are not constant regarding strike and dip. Ore bodies do not have natural geological boundaries; their contours are determined by sampling data. The internal structure of the ore bodies is complex, with intermittent mineralization, and barren “windows” are noted. The permanent minerals of the ore bodies are quartz and sulfides, which are associated with gold mineralization. Over the course of previous prospecting and appraisal work at the Dobroe deposit, eight ore bodies were identified and territorially united into ore blocks, including Dobry, Alexandriisky, and Tatyansky. Samples for the study of fluid inclusions in quartz and sulfides were taken from ore body No. 5.

Quartz is a constant mineral of the Dobroe deposit. There are two varieties of quartz: Quartz 1 and Quartz 2 (Figure 2a). Microscopically, Quartz 1 grains are transparent, equidimensional polygons with rectilinear outlines. These grains form a granoblastic honeycomb texture. The grain sizes range from 0.05 to 0.3 mm.

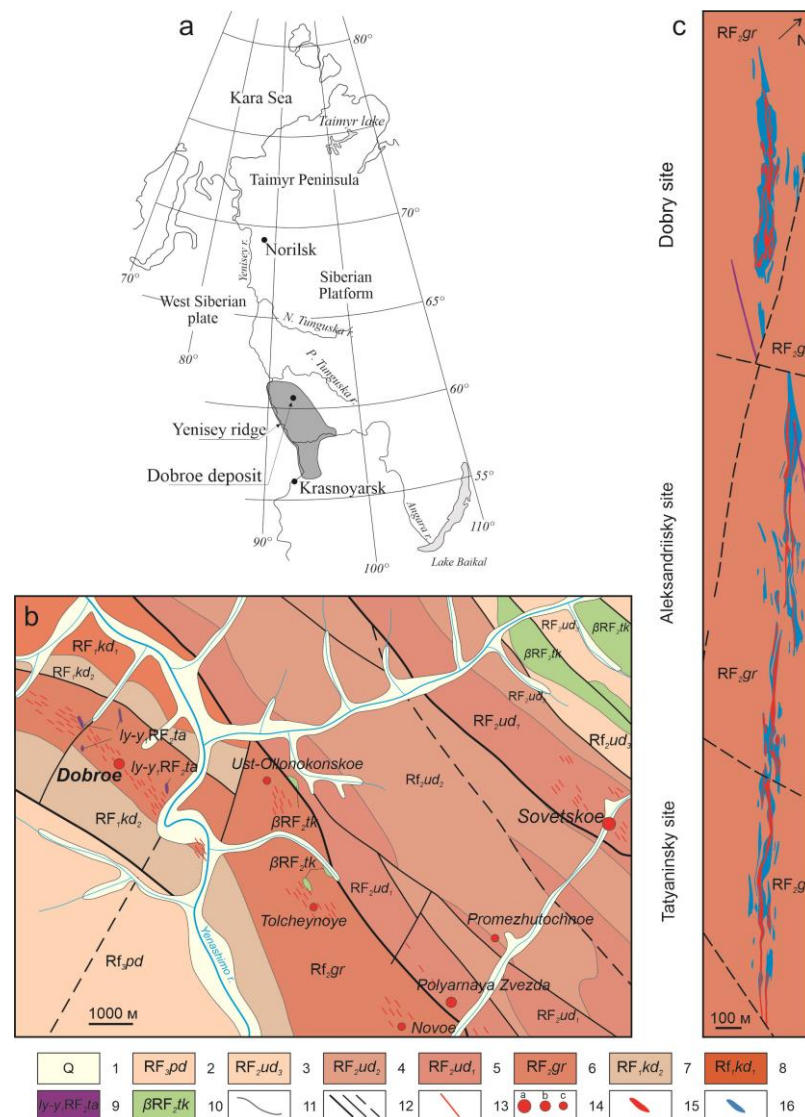


Figure 1. (a) Geographic location of the Dobroe gold deposit; (b) geological map of the Sovetsky ore cluster; (c) geological map of the Dobroe deposit. 1—Quaternary sediments; 2—Podmskaya suite (dolomites, limestones); 3—upper Uderey subformation (argillaceous phyllitized schists); 4—middle Uderey subformation (phyllitized shales, phyllites); 5—lower Uderey subformation (carbonaceous phyllites); 6—Gorbilok formation (quartz-sericite-chlorite schists); 7—upper Corda subformation (metasiltstones, sandstones, chlorite-biotite schists); 8—lower Corda subformation (marbles, marmorized limestones); 9—granites of the Tatar-Ayakhta complex; 10—dolerites of the Tokma complex; 11—geological boundaries; 12—tectonic disturbances: regional, proved, expected; 13—veined silicified and sericite metasomatites; 14—gold deposits ((a) >100 t, (b) 10–100 t, (c) <10 t); 15—ore bodies; 16—mineralized zones.

Quartz 2 forms aggregates of >2–3 mm irregular grains with sinuous outlines and fills the space in between Quartz 1 aggregates. The color of these grains varies from light gray to gray. In most cases, large individual grains or vein aggregates of this quartz are located in the central parts of veins and lenses, the selvages of which are composed of metasomatic honeycomb quartz. Quartz 2 occurs more often in the ore zone of the deposit than in the barren zone.

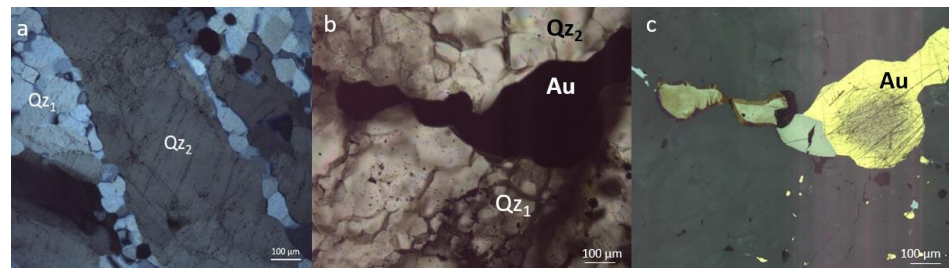


Figure 2. Different types of quartz from the Dobroe deposit: (a) granoblastic (Qz_1) and vein (Qz_2) quartz, (b) quartz with native gold in transmitted light, (c) quartz with native gold in reflected light.

The ores contain calcite, siderite, and chlorite, as well as ore minerals which form nested dissemination and fissure segregations. The content of ore minerals does not exceed 5%, and the distribution of those in ores is extremely uneven. The early association of sulfides consists of pyrrhotite, arsenopyrite, and pyrite. Late association (chalcopyrite, galena, ulmanite, and Bi-Te minerals) in a subordinate amount forms microscopic segregations in quartz veins. Ore minerals are also found in the host schists as layered, disseminated aggregates, thin veinlets, and dispersed, fine, crystalline, granular dissemination.

Microscopic (0.X–0.00X mm) and larger (>1 mm) visible native gold form primarily in quartz veins as fractured, lamellar, and vein-like segregations (Figure 2b,c). Gold resulting from early association presents in the form of intergrowths with sulfides (pyrrhotite, arsenopyrite), as well as fracture segregations with subisometric inclusions in them (Figure 3a–c). Late gold has been found to be associated with galena and bismuth minerals (native bismuth and hedleyite) (Figure 3e,f). Regularly, late sulfides and gold form rims at the boundaries of pyrrhotite, arsenopyrite, and quartz. Similar intergrowths with early sulfides make up galena-bismuth-ulmanite aggregates which lack visible gold (Figure 3d).

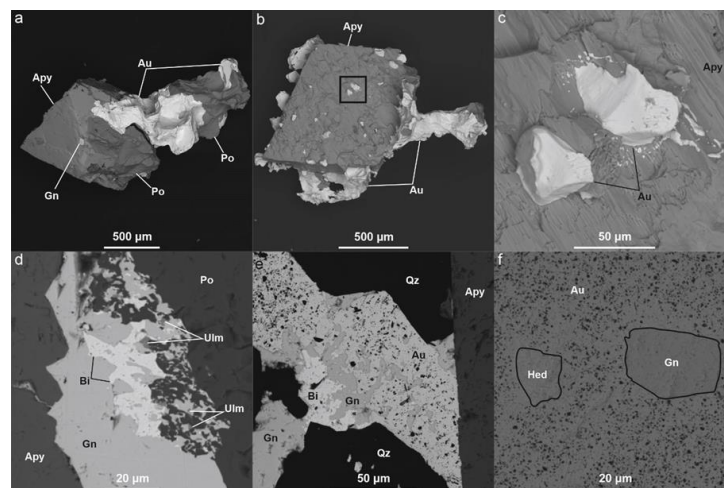


Figure 3. Ore associations of the Dobroe deposit: (a) intergrowth of arsenopyrite (Apy), crystal of pyrrhotite (Po) and gold (Au); (b) gold inclusions in arsenopyrite crystal; (c) enlarged area from (b); (d) intergrowths of galena (Gn), native bismuth (Bi), and ulmanite (Ulm) at the contact of pyrrhotite and arsenopyrite; (e) gold-bismuth-galena aggregate at the boundary of arsenopyrite and quartz (Qz); (f) inclusions of hedleyite (Hed) and galena (the contours of the inclusions are highlighted) in native gold.

The fineness of native gold varies from 838 to 913‰, with an average value of ~900. The main impurity element is silver. The silver contents of gold of the galena-bismuth and pyrrhotite-arsenopyrite associations do not differ significantly; however, a decrease in the silver content (from ~10 wt.% to ~8 wt.%) of gold following contact with galena was observed.

Gold reserves at the Dobroe deposit do not exceed 10 t; at the Tatyansky site, they are less than 1 t [3,4].

3. Samples and Methods

We studied a collection of samples taken from across ore body No. 5 (RL 4.3) from horizons 380–390 (Figure 1) of the Tatyansky site of the Dobroe deposit. Six samples were collected from the barren zone, and the gold content in them did not exceed 0.1 g/t. From within the ore zone, where a gold content of more than 1.4 g/t was recorded, 15 samples were selected and studied. All samples were quartz-sulfide aggregates enclosed in a schist rim. The schist's xenoliths and sulfide inclusions were visible in the quartz. Sulfides often form nests and veinlets in the form of arsenopyrite, pyrite, pyrrhotite, and chalcopyrite. We used half of the sample to make doubly polished thin sections for studying individual fluid inclusions (FIs). The second half was crushed and forced through a sieve. Pure quartz and sulfides without visible impurities were picked using a binocular magnifying glass.

Electron microscopy studies were performed on the SEM Tescan Vega III SBH with EDX Oxford X-Act at the R&D Nornickel Center, SibFU, Krasnoyarsk.

For individual fluid inclusions in quartz, the temperatures of general homogenization were measured, and the type of homogenization was observed—into the liquid or vapor phase. In the aqueous phase of the inclusions, the eutectic and ice melting temperatures were measured. In the gas phase of the inclusions, the temperatures of partial homogenization and the melting of liquefied gases were measured, and the type of homogenization was also noted—into the liquid or vapor phase. The measurements were carried out in a TH-MSG-600 microthermal chamber by Linkam with a measurement range of -196 to $+600$ °C. The standard instrumental measurement accuracy was ± 0.1 °C in the negative and ± 5 °C in the positive temperature range.

Fluid pressure in the hydrothermal system was calculated from syngenetic inclusions (type A ($L_{H_2O} + V(L)_{CO_2 \pm CH_4 \pm N_2}$) and type B ($V(L)_{CO_2 \pm CH_4 \pm N_2}$)) according to the methods given in [40–43].

The salinity of the aqueous phase of fluid inclusions was estimated from the melting temperature of ice using a two-component water–salt system NaCl–H₂O [44] through an equivalent of NaCl, wt.%. The compositions of the aqueous phases of individual inclusions were determined based on the measured eutectic temperatures, which characterize the water–salt system [45].

The compositions of the gas phases of individual fluid inclusions in quartz were analyzed via a Raman spectroscopy on a single-channel Horiba J.Y. LabRAM HR800 Raman spectrometer equipped with an argon laser, which was 1.5 μ m in diameter and had 0.75 W of power, according to the methods described in [46–48].

The bulk compositions of fluids in quartz and sulfides were determined via a pyrolysis-free coupled gas chromatography–mass spectrometry (GC–MS) using a Focus GS/DSQ II Series Single Quadrupole MS analyzer (Thermo Scientific, Waltham, MA, USA). When preparing samples for analysis, no acids, solvents, or organic substances were used which could distort the initial composition of the extracted fluid. The sample preparation procedure for analysis excluded its contact with any solvents or other possible contaminants. Input of the mixture extracted from the sample during the shock crushing was carried out online in the He flow without concentration, including cryofocus. This method does not pyrolyze the sample but heats it, only in order to convert any water within the sample into the gas phase. In this case, it is a gas mixture that is analyzed in situ rather than pyrolyzate, which contains more oxidized compounds (H₂O, CO, CO₂, etc.) due to the reactions between the gas mixture compounds, between the gas mixture and accumulator surface, and between the gas phase compounds and the sample. Blank online analyses were carried out before and after the “working” analysis. The previous analysis made it possible to control the release of gases absorbed by the sample surface, including atmospheric components, and to record the system blank at the end of the process. The degree and completeness of hydrocarbon and polycyclic aromatic hydrocarbon elution from the analytical column

during temperature programming in a chromatograph thermostat were determined using the results of subsequent analysis. If necessary, the analytical column was thermoconditioned to achieve the required blank. The collected spectra were interpreted both manually and using the AMDIS 2.73 (Automated Mass Spectral Deconvolution and Identification System) software, with background correction against spectra from the NIST 2020 and Wiley Registry 12th Edition Mass Spectral libraries (NIST MS Search 2.4). Peak areas in chromatograms were determined using the ICIS algorithm Xcalibur (1.4SR1 Qual Browser). This method is suitable for the detection of trace volatile concentrations exceeding tens of femtograms. The relative concentrations (rel. %) of volatile components in the studied mixture were obtained by normalizing the areas of individual chromatographic peaks to the total area of all peaks. The GC–MS analysis technique is described in detail by [36,49].

The sulfur isotopes ($\delta^{34}\text{S}$) of sulfides were measured in the SO_2 gas obtained during the interaction of sulfides with CuO at 1000 C and normalized to the isotope composition of troilite from the Canyon Diablo meteorite. The reproducibility of $\delta^{34}\text{S}$ values, including sample preparation, was 0.1% [50].

The isotope composition ($\delta^{13}\text{C}$) of carbon dioxide in fluid inclusions from quartz was determined in the gas extracted from 1000 mg samples by decrepitation at 600 °C. CO_2 was bound at the temperature of liquid nitrogen, after which the cryo trap was isolated from the vacuum line. The ampules with CO_2 were analyzed using a ThermoFinnigan Delta Plus–XP mass spectrometer equipped with the double inlet system. The results were normalized using the VPDB (Pee Dee Belemnite) standard.

Microthermometric, Raman, and GC–MS analyzes were performed at the Laboratory of Thermobarogeochemistry, IGM SB RAS. Isotopic analyzes were carried out at the Analytical Center for Multi-Elemental and Isotope Research SB RAS.

4. Results

4.1. Fluid Inclusion Types

Individual fluid inclusions were studied in Quartz 1 and Quartz 2 (Figure 4) from lenses, veinlets, and veins hosted by green schists of the barren and ore zones. According to the phase and chemical composition, two types (A and B) of fluid inclusions in quartz were distinguished. Type A is represented by two-phase water–carbon dioxide ($\text{L}_{\text{H}_2\text{O}} + \text{V}(\text{L})_{\text{CO}_2 \pm \text{CH}_4 \pm \text{N}_2}$) inclusions (Figure 4a) with varying ratios of water and gas. The forms of vacuoles of this type of inclusions are the most diverse; their sizes do not exceed 10–15 μm . Type B are single-phase vapor or liquid carbon dioxide–hydrocarbon inclusions ($\text{V}(\text{L})_{\text{CO}_2 \pm \text{CH}_4 \pm \text{N}_2}$) (Figure 4b). In transmitted light under a microscope, these inclusions are dark (sometimes black), have the most diverse but more often elongated shape of vacuoles, and are two to three times larger than type A inclusions.

In Quartz 1, both from the barren and ore zones, primary and pseudosecondary generations of inclusions were practically absent. It contained mainly secondary generations of fluid inclusions confined to microcracks, sometimes mutually intersecting, crossing the grain boundaries of granoblastic Quartz 1 (Figure 4d).

In some cracks, there were inclusions of type A (water–carbon dioxide); in others, these were of type B (carbon dioxide–hydrocarbon) (Figure 4d).

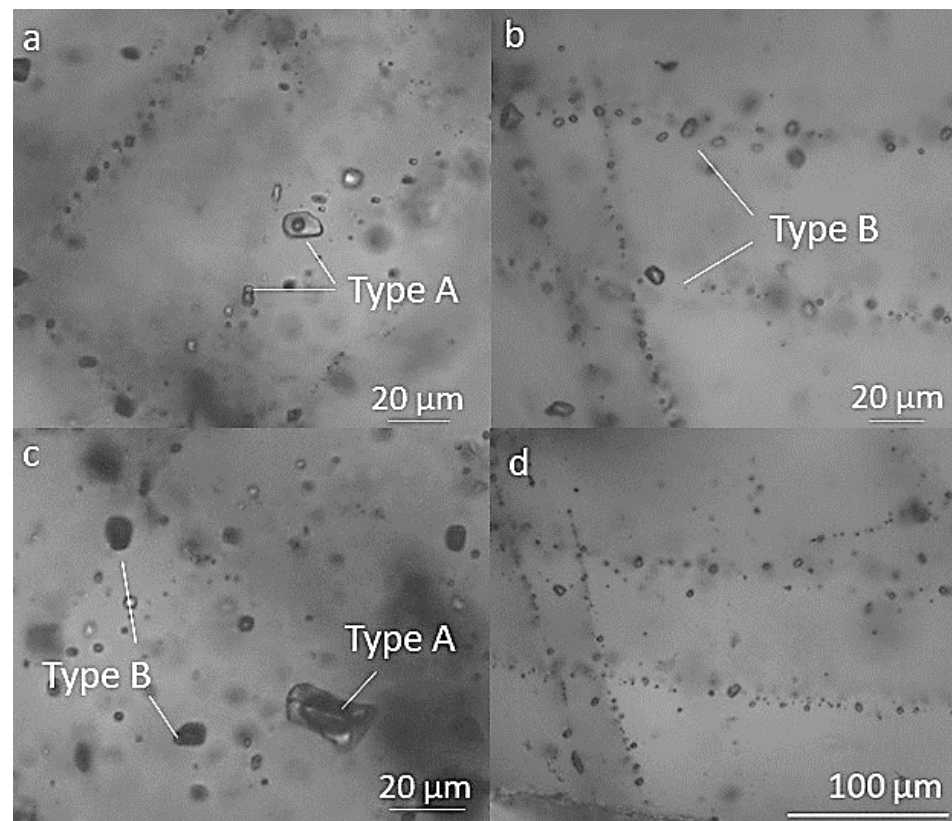


Figure 4. Types of fluid inclusions in quartz from the Dobroe deposit: (a) type A, $L_{H_2O} + V(L)CO_2 \pm CH_4 \pm N_2$; (b) type B, $(V(L)CO_2 \pm CH_4 \pm N_2)$, (c) coexisting type A and type B fluid inclusions; (d) systems of intersecting fractures filled with type B inclusions.

In Quartz 2, fluid inclusions were represented by primary, pseudosecondary, and secondary generations. Primary and pseudosecondary generations of inclusions are located inside quartz grains as separate, isolated formations or groups of five to ten inclusions not associated with cracks. Secondary generations are inclusions associated with healed microcracks that cross the boundaries of quartz grains (Figure 4).

Quartz 2 contained both types (A and B) of fluid inclusions (Figure 4c, which differ in phase and chemical composition). The ratio between water–carbon dioxide (type A) and carbon dioxide–hydrocarbon (type B) types of fluid inclusions in Quartz 2 was varied. In one group of primary inclusions filled with water–carbon dioxide fluid, there were also single-phase carbon dioxide–hydrocarbon inclusions (type B). More frequently, type B inclusions were confined to mutually intersecting microcracks both inside and outside the quartz grains (Figure 4d).

4.2. Homogenization Temperatures, Salinity, and Pressure of Fluid

The results of microthermometric studies of fluid inclusions in quartz of the Dobroe deposit are presented in Table 1. Since there were practically no primary fluid inclusions in Quartz 1, Table 1 shows the results of thermometric measurements in inclusions of secondary generations. The homogenization temperature of these inclusions from the barren zone ($Au < 0.1$ g/t) ranged from 180 to 320 °C with homogenization into the liquid or gas phase. These inclusions trapped fluid with a salinity of 1.5–9.0 wt.%, NaCl-eq. The composition of the aqueous phase is determined by Mg and Na chlorides. This is indicated by the eutectic temperatures, which ranged from −23.6 to −36.5 °C. In the secondary generations of inclusions, where the water phase prevailed over the gas phase, the temperature of general homogenization did not exceed 210 °C when homogenized into a liquid, and the salinity of the fluid did not exceed 3.0 wt.%, NaCl-equiv. In single-

phase (type B) secondary inclusions in Quartz 1, the melting temperature of the phase that formed during cooling ranged from -72.0 to -83.0 °C with a temperature of partial homogenization into vapor and liquid ranging from -10.5 to -140.6 °C. The fluid pressure ranged from 0.2 to 0.8 kbar.

In Quartz 2 of the gold-bearing zone ($Au = 1.4$ g/t), the temperature of the general homogenization of primary and pseudosecondary water–carbon dioxide (type A) inclusions ranged from 240 to 360 °C for homogenization into both liquid and vapor. The fluid salinity reached 15.0 wt.%, NaCl-equiv. Fluid pressure varied between 0.8 and 1.3 kbar. When the temperature dropped below 0 °C, a phase where melting temperatures ranged from -63.8 to -80.4 °C occurred in the gas bubble of inclusions (type A), at a temperature of partial homogenization ranging from -3.1 to -28.4 °C, homogenization occurred into gas and into liquid. In pseudosecondary and secondary generations of single-phase carbon dioxide–hydrocarbon fluid inclusions (type B), fluid is trapped, with a melting temperature of the phase formed during cooling ranging from -69.8 to -89.6 °C and a partial homogenization temperature ranging from -8.2 up to -93.6 °C. In most type B inclusions, homogenization occurred into the vapor phase.

Secondary vapor–liquid inclusions, where the liquid water phase prevailed over the gas one ($L_{H_2O} \gg V$), homogenized only into the liquid phase within the temperature range of 110 to 230 °C, while salinity varied from 1.5 to 2.5 wt.% NaCl eq.

4.3. Composition of Fluid Inclusions in Quartz and Sulfides

The composition of the gas phase of 48 individual inclusions in quartz was determined using a Raman spectroscopy (Table 2, Figure 5). The composition of the gas phase of the fluid revealed the presence of three main components: CO_2 , CH_4 , and N_2 , the content of which varied over a wide range.

Water–carbon dioxide (A) inclusions from the barren and ore zones were dominated by CO_2 , while carbon dioxide–hydrocarbon type (B) inclusions were dominated by CH_4 and N_2 (Figure 6). In inclusions (type A) where the water phase was constantly present, the CO_2/CH_4 ratio averaged 31.0 ($n = 28$). In inclusions filled with carbon dioxide–hydrocarbon fluid (type B), the CO_2/CH_4 ratio was lower and averaged 4.2 ($n = 18$).

The bulk compositions of volatiles in fluid inclusions were determined via a GC–MS of fluid inclusions from 12 samples of quartz and sulfides (Table 3, Supplementary Tables S1–S12). Table 3 shows the most representative results of GC–MS analysis of volatiles of samples from the gold-bearing and barren zones and analyses of all samples were used for Figure 7. Water, carbon dioxide, and a wide range of hydrocarbons and their derivatives, as well as nitrogen- and sulfur-chlorinated compounds, were found in the composition of volatiles in the fluid (Figures 8–10). The total number of detected components in sulfides ranged from 133 to 148, and in quartz it reached 202.

Table 1. Summary of fluid inclusion microthermometric data from the Dobroegold deposit.

FI Type	T _h Total, °C	Type of Homogenization	T _{eut} , °C	T _m , °C	Salinity, wt.%, NaCl-eq.	T _m of CO ₂ ±CH ₄ ±N ₂ , °C	Partial T _h , °C	Type of Homogenization	P, kbar
Gold-bearing zone, Au > 1.4 g/t									
P, PS L _{H₂O} + V	$\frac{240-360}{320}$ (44)	L, V	$\frac{-23.6 \div -32.0}{-30.8}$ (9)	-2.0 ÷ -10.0 (8)	4.5–15.0	-63.8 ± -80.4	-3.1 ± -28.4	L, V	0.8–1.3
PS, S L(V)CO ₂ ±CH ₄ ±N ₂	–	–	–	–	–	-69.8 ± -89.6	-8.2 ± -93.6	L, V	
S L _{H₂O} + V	$\frac{110-230}{200}$ (16)	L	$\frac{-19.3 \div -24.0}{-21.4}$ (5)	-0.5 ÷ -1.5 (5)	1.5–2.5	–	–	–	
Barren zone, Au < 0.1 g/t									
S L _{H₂O} + V	$\frac{180-320}{280}$ (15)	L, V	$\frac{-20.7 \div -29.5}{-24.8}$ (7)	-0.7 ÷ -5.0 (5)	1.5–9.0	-57.6 ± -71.2	-1.5 ± -8.3	L, V	0.2–0.8
S L(V)CO ₂ ±CH ₄ ±N ₂	–	–	–	–	–	-72.6 ± -83.0	-10.5 ± 140.6	L, V	
S L _{H₂O} + V	$\frac{120-210}{190}$ (11)	L	$\frac{-17.5 \div -19.8}{-18.0}$ (5)	-0.3 ÷ -1.5 (5)	0.5–3.0	–	–	–	

Note: FI types: P—primary, PS—pseudosecondary, S—secondary; T_h—homogenization temperature; types of homogenization: L—to liquid, V—to vapor; T_{eut}—eutectic temperature, T_m—melting temperature, P—pressure. In parenthesis—number of measurements.

Table 2. Microthermometric characteristics and compositions of the gas phases of individual primary and pseudosecondary fluid inclusions in quartz of the Dobroe gold deposit (Raman spectroscopy data).

No.	T_{m} , °C	T_{h} , °C	Type of Homogenization	Content, mol. %			CO_2/CH_4
				CO_2	CH_4	N_2	
FI type A ($L_{H_2O}+L(V)_{CO_2\pm CH_4\pm N_2}$)							
D-1-1/18	-71.3	-28.4	V	82.0	17.0	1.0	48.0
D-1-1/20	-70.8	-5.0	L	53.0	10.0	37.0	5.3
D-1-1/21	-69.3	-6.1	V	50.0	10.0	40.0	5.0
D-1-1/22	-74.3	-6.9	V	47.0	11.0	42.0	4.3
D-6/1	-75.4	-7.8	L	47.0	7.6	45.4	6.2
D-6/2	-80.4	-9.3	V	94.2	1.3	4.5	72.5
D-6/3	-69.8	-7.4	V	62.6	22.6	14.8	2.8
D-6/4	-58.4	-9.3	L	80.0	1.2	18.8	66.7
D-6/5	-63.8	-3.1	V	60.7	3.7	35.6	16.4
D-2-5-a	-	-	-	39.6	7.3	53.1	5.4
D-2-5-f	-	-	-	22.8	1.4	75.8	16.3
D-6-d	-	-	-	98.8	0.3	0.9	329.3
D-1-3/2	-62.5	-3.6	L	71.5	22.9	5.6	3.1
D-1-3/3	-59.8	-8.3	V	54.1	14.1	31.8	3.8
D-1-3/4	-57.6	-11	V	91.4	8.6	-	10.3
D-1-3/7	-66.3	-4.2	L	78.0	20.0	2.0	3.9
D-1-3/9	-71.2	-1.5	L	94.0	4.0	2.0	23.5
D-1-3/10	-63.6	-4.5	V	76.4	23.2	0.4	3.3
D-1-5/1	-59.9	-3.8	L	81.7	6.7	11.6	12.2
D-1-5/2	-65.8	-5.1	V	91.3	7.3	1.4	12.5
D-1-5/3	-63.4	-4.9	V	93.0	5.9	1.1	15.8
D-1-5/4	-	-	-	93.8	2.3	3.9	40.8
D-1-5/6	-61.3	-6.1	L	98	0.7	1.3	140
D-1-5/7	-	-7.3	V	45.9	6.0	48.1	7.6
D-1-5/11	-64.1	-4.3	V	41.0	24.0	35.0	1.7
D-1-5/13	-66.5	-6.3	L	43.8	16.2	40.0	2.7
D-1-5/14	-69.8	-5.1	V	72.0	14.0	14.0	5.1
D-1-5/15	-68.3	-6.5	V	75.9	23.0	1.1	3.3
FI type B ($L(V)_{CO_2\pm CH_4\pm N_2}$)							
D-1-9/4	-	-93.6	V	3.6	5.7	90.7	0.6
D-1-8/19	-89.6	-8.2	V	9.0	89.0	2.0	0.1
D-1-8/29	-	-122.1	V	15.0	16.0	69.0	0.9
D-2-5/3	-69.8	-14.8	L	35.8	17.5	32.1	2.0
D-6/7	-72.3	-15	L	43.6	36.8	19.6	1.2
D-6/8	-	-89.3	V	16.3	8.1	75.6	2.0
D-6/9	-	-91.4	L	15.2	8.7	76.1	1.7
D-2-5-b	-	-	-	17.7	2.8	79.5	6.3
D-2-5-e	-	-	-	13.1	2.6	84.3	5.0
D-6-b	-	-	-	39.7	1.9	58.4	20.9
D-6-c	-	-	-	54.9	1.8	43.3	30.5
D-1-3/1	-	-123.5	V	4.0	15.0	81.0	0.3
D-1-3/2	-	-140.6	V	13.0	15.0	72.0	0.9
D-1-3/4	-	-135.2	L	12.0	18.0	70.0	0.7
D-1-3/5	-	-93.0	V	15.0	29.0	56.0	0.5
D-1-3/8	-	-89.0	V	4.0	90.0	6.0	0.04
D-1-3/16	-83.0	-13.0	L	35.0	65.0	-	0.5
D-1-3/17	-82.6	-10.5	L	37.0	63.0	-	0.6

T_h —homogenization temperature; types of homogenization: L—to liquid, V—to vapor; T_m —melting temperature.

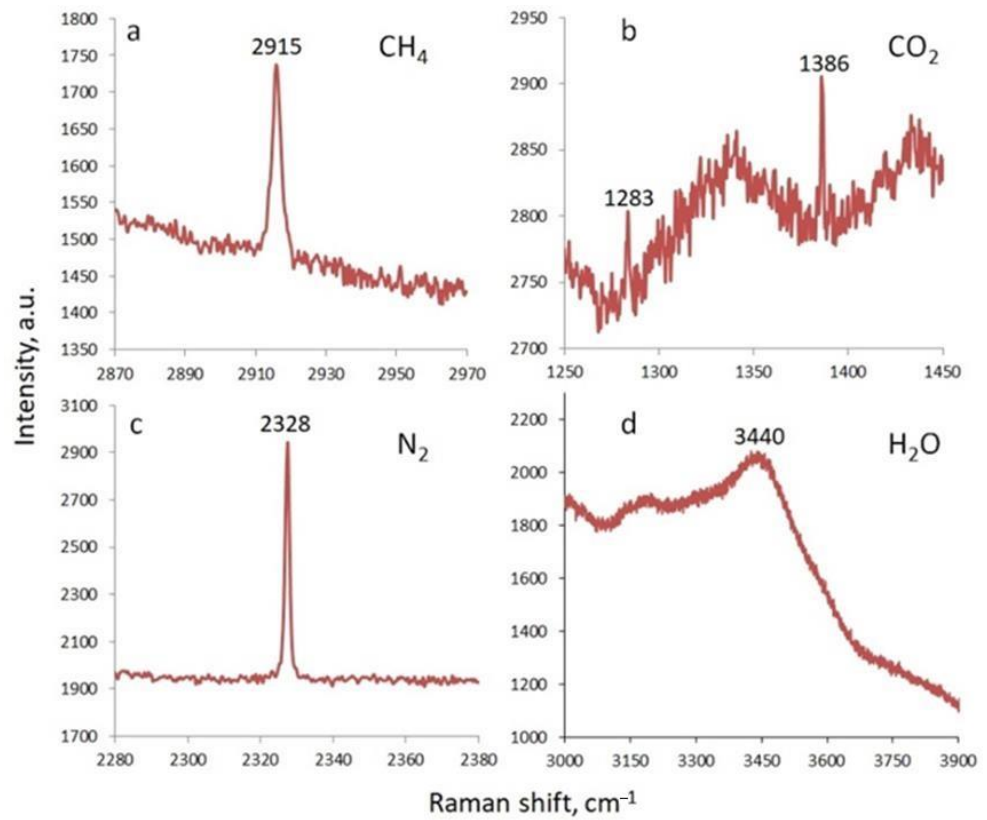


Figure 5. Raman spectra of the gas (a–c) and water (d) phases of fluid inclusions in quartz from the Dobroe deposit.

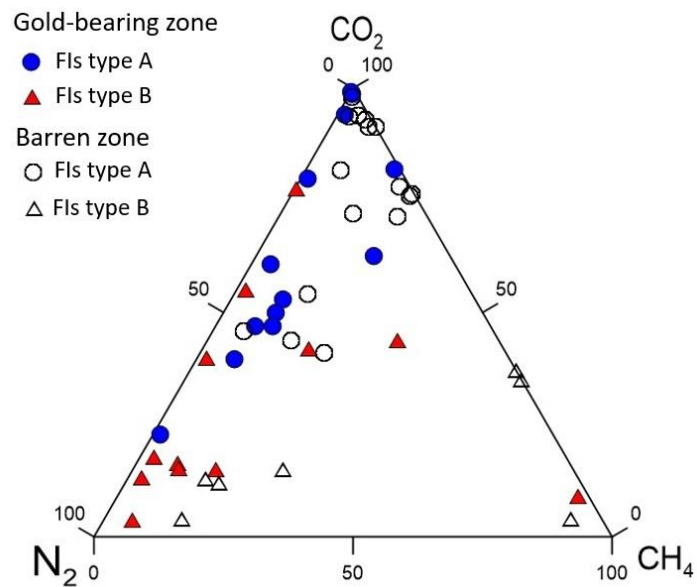


Figure 6. Compositions of the gas phases of fluid inclusions in quartz from the Dobroe gold deposit (Raman spectroscopy data).

Table 3. Content (rel.%) and number (in parentheses) of volatiles extracted via mechanical shock destruction of minerals from the Dobroe deposit (according to a GC–MS).

Component	Gold-Bearing Zone, Au > 1.4 g/t				Barren Zone, Au < 0.1 g/t		
	D–10		D–2–12		D–1–2	D–1–3	
	Arsenopyrite	Quartz 2	Quartz 1	Arsenopyrite	Quartz 1	Quartz 2	Quartz 1
		Aliphatic hydrocarbons					
Paraffins (alkanes)	6.31 (13)	0.30 (11)	2.03 (16)	2.31 (13)	1.49 (13)	1.57 (19)	4.40 (16)
Olefins (alkenes)	0.20 (16)	0.07 (15)	0.55 (14)	0.27 (20)	0.36 (17)	1.28 (31)	0.12 (24)
		Cyclic hydrocarbons					
Cycloalkanes, cycloalkenes, arenes, PAH	0.43 (12)	0.06 (10)	0.57 (9)	0.25 (15)	0.42 (12)	0.23 (21)	0.15 (19)
		Oxygenated hydrocarbons					
Alcohols, ethers, and esters	0.51 (16)	0.81 (18)	1.82 (18)	1.49 (14)	2.90 (20)	0.27 (24)	2.12 (26)
Aldehydes	0.79 (20)	0.18 (22)	4.62 (23)	0.30 (2)	0.99 (23)	0.43 (22)	0.65 (23)
Ketones	0.75 (17)	0.26 (16)	2.21 (17)	0.30 (16)	1.09 (18)	0.29 (21)	0.43 (20)
Carboxylic acids	0.17 (13)	0.78 (11)	1.71 (9)	1.44 (19)	3.18 (12)	0.62 (13)	0.56 (13)
		Heterocyclic compounds					
Dioxanes, furans	0.14 (6)	0.01 (8)	0.18 (11)	0.09 (8)	0.11 (11)	0.02 (10)	0.01 (7)
		Nitrogenated compounds					
N ₂ , ammonia, nitriles	0.96 (9)	12.31 (10)	13.48 (12)	0.89 (10)	46.9 (13)	37.58 (22)	34.07 (23)
		Sulfonated compounds					
H ₂ S, SO ₂ , CS ₂ , COS, thiophenes	2.19 (9)	0.03 (8)	2.30 (10)	0.08 (9)	0.34 (8)	0.75 (16)	0.71 (15)
		Inorganic compounds					
CO ₂	52.34	58.13	32.85	26.36	38.80	10.75	45.77
H ₂ O	34.16	27.09	37.68	66.23	3.38	47.21	10.96
Ar	–	–	–	–	–	0.02	0.03
Number of components	133	131	141	128	149	202	188
Alkanes/alkenes	31.5	3.0	3.3	7.7	3.8	1.2	36.7
CO ₂ /(CO ₂ + H ₂ O)	0.6	0.7	0.5	0.3	0.9	0.2	0.8
Σ(C ₅ –C ₁₇)/Σ(C ₁ –C ₄)	0.02	0.28	1.24	0.04	0.34	1.27	0.03
H/(H + O)	0.58	0.44	0.60	0.63	0.44	0.65	0.50

Note: The relative concentrations (rel.%) of volatile components in the mixture under study were obtained by normalizing the areas of individual chromatographic peaks to the total area of all peaks.

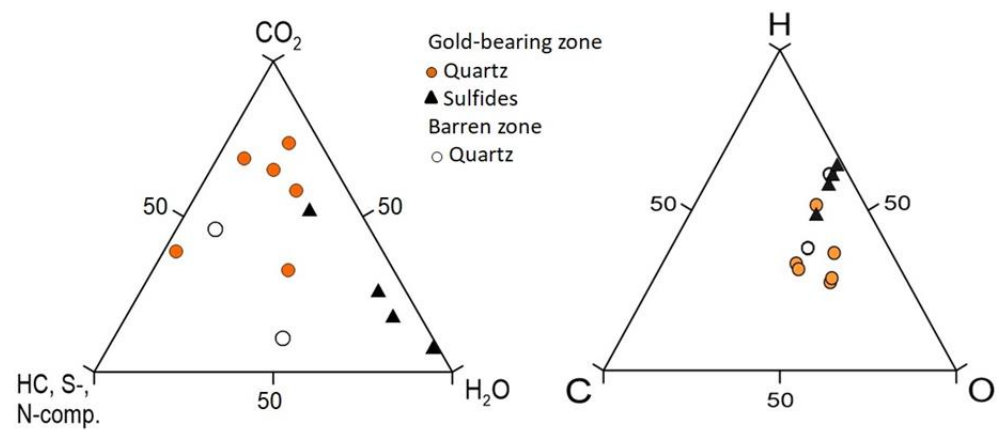


Figure 7. Composition volatiles extracted from fluid inclusions in quartz and sulfides from the Dobroe deposit (GC–MS data).

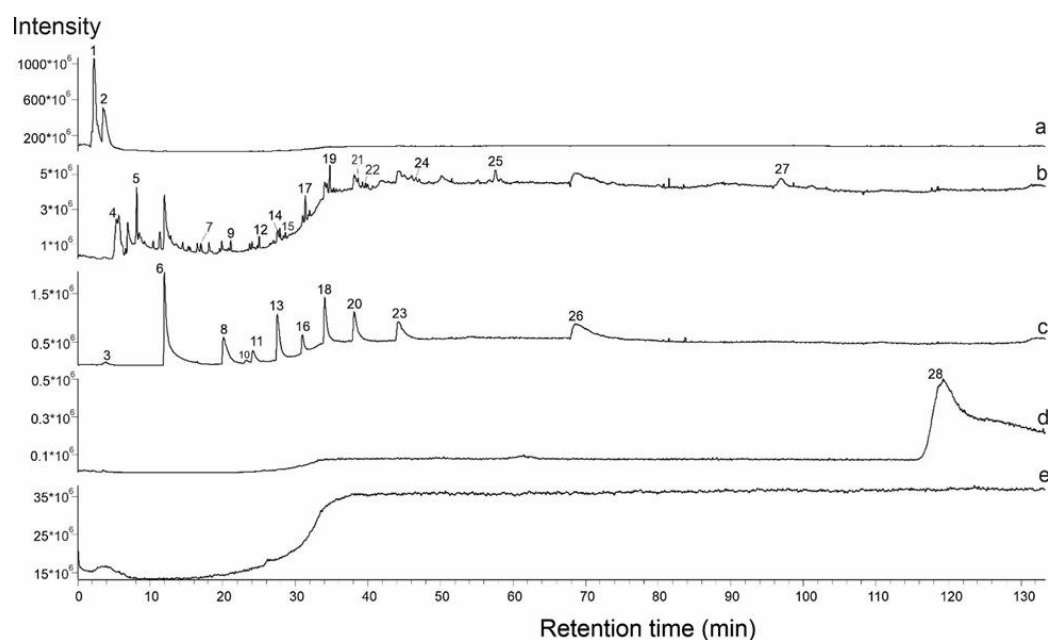


Figure 8. Results of a GC–MS analysis of volatiles extracted via mechanical shock crushing from quartz D10 of the Dobroe deposit. Total ion chromatogram (TIC) (a) and reconstructed ion chromatograms (RIC) for m/z (43 + 57 + 71 + 85) (b), m/z 60 (c), m/z 149 (d), and blank (TIC) (e). 1—Carbon dioxide (CO_2); 2—water (H_2O); 3—Carbonyl sulfide (COS); 4—Acetaldehyde ($\text{C}_2\text{H}_4\text{O}$); 5—2-Propanone ($\text{C}_3\text{H}_6\text{O}$); 6—Acetic acid ($\text{C}_2\text{H}_4\text{O}_2$); 7—n-Heptane (C_7H_{16}); 8—n-Butanoic acid ($\text{C}_4\text{H}_8\text{O}_2$); 9—n-Octane (C_8H_{18}); 10—3-Methylbutanoic acid ($\text{C}_5\text{H}_{10}\text{O}_2$); 11—n-Pentanoic acid ($\text{C}_5\text{H}_{10}\text{O}_2$); 12—n-Nonane (C_9H_{20}); 13—n-Hexanoic acid ($\text{C}_6\text{H}_{12}\text{O}_2$); 14—n-Octanal ($\text{C}_8\text{H}_{16}\text{O}$); 15—n-Decane ($\text{C}_{10}\text{H}_{22}$); 16—n-Heptanoic acid ($\text{C}_7\text{H}_{14}\text{O}_2$); 17—n-Nonanal ($\text{C}_9\text{H}_{18}\text{O}$); 18—n-Octanoic acid ($\text{C}_8\text{H}_{16}\text{O}_2$); 19—n-Decanal ($\text{C}_{10}\text{H}_{20}\text{O}$); 20—n-Nonanoic acid ($\text{C}_9\text{H}_{18}\text{O}_2$); 21—2-Undecanone ($\text{C}_{11}\text{H}_{22}\text{O}$); 22—1-Tridecene ($\text{C}_{13}\text{H}_{26}$); 23—n-Decanoic acid ($\text{C}_{10}\text{H}_{20}\text{O}_2$); 24—1-Tetradecene ($\text{C}_{14}\text{H}_{28}$); 25—1-Pentadecene ($\text{C}_{15}\text{H}_{30}$); 26—n-Dodecanoic acid ($\text{C}_{12}\text{H}_{24}\text{O}_2$); 27—2-Pentadecanone ($\text{C}_{15}\text{H}_{30}\text{O}$); 28—Dipropyl phthalate ($\text{C}_{14}\text{H}_{18}\text{O}_4$).

The compositions of volatiles from fluid inclusions in Quartz 1 and Quartz 2 were dominated by CO_2 , which made up 60–70 rel.% with fluctuations ranging from 10.7 to 73.8 rel.%. The proportion of water in these inclusions was lower and averaged 21.9 rel.% ($n = 8$). The content of hydrocarbons represented by aliphatic, cyclic, and oxygenated compounds averaged 16.3 rel. % ($n = 8$), and that of sulfides was 7.4 rel.% ($n = 5$).

Of particular note was the high proportion (up to 47 rel.%) of nitrogenated compounds in fluid inclusions from quartz (Table 3, samples D–2–12; D–1–2; D–1–3). In these samples, 23 chemical compounds were identified among nitrogenated compounds, which is almost two times more than the number found in sulfides (Table 3). In nitrogenated compounds, molecular nitrogen (N_2) predominated, the proportion of which was 80%–90%.

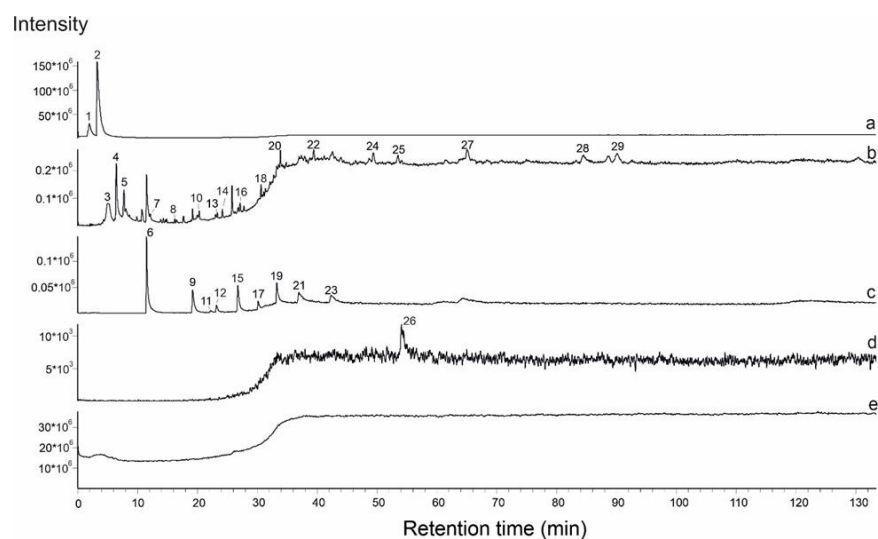


Figure 9. Results of a GC–MS analysis of volatiles extracted via mechanical shock crushing from arsenopyrite D10 of the Dobroe deposit. Total ion chromatogram (TIC) (a) and reconstructed ion chromatograms (RIC) for m/z (43 + 57 + 71 + 85) (b), m/z 60 (c), m/z 149 (d), and blank (TIC) (e). 1—Carbon dioxide (CO_2); 2—Water (H_2O); 3—Acetaldehyde ($\text{C}_2\text{H}_4\text{O}$); 4—Ethanol ($\text{C}_2\text{H}_6\text{O}$); 5—2-Propanone ($\text{C}_3\text{H}_6\text{O}$); 6—Acetic acid ($\text{C}_2\text{H}_4\text{O}_2$); 7—*n*-Hexane (C_6H_{14}); 8—*n*-Heptane (C_7H_{16}); 9—*n*-Butanoic acid ($\text{C}_4\text{H}_8\text{O}_2$); 10—*n*-Octane (C_8H_{18}); 11—3-Methylbutanoic acid ($\text{C}_5\text{H}_{10}\text{O}_2$); 12—*n*-Pentanoic acid ($\text{C}_5\text{H}_{10}\text{O}_2$); 13—*n*-Nonane (C_9H_{20}); 14—2-Methyl-6-heptanone ($\text{C}_8\text{H}_{16}\text{O}$); 15—*n*-Hexanoic acid ($\text{C}_6\text{H}_{12}\text{O}_2$); 16—*n*-Octanal ($\text{C}_8\text{H}_{16}\text{O}$); 17—*n*-Heptanoic acid ($\text{C}_7\text{H}_{14}\text{O}_2$); 18—*n*-Nonanal ($\text{C}_9\text{H}_{18}\text{O}$); 19—*n*-Octanoic acid ($\text{C}_8\text{H}_{16}\text{O}_2$); 20—*n*-Decanal ($\text{C}_{10}\text{H}_{20}\text{O}$); 21—*n*-Nonanoic acid ($\text{C}_9\text{H}_{18}\text{O}_2$); 22— γ -Nonalactone ($\text{C}_9\text{H}_{16}\text{O}_2$); 23—*n*-Decanoic acid ($\text{C}_{10}\text{H}_{20}\text{O}_2$); 24—*n*-Pentadecane ($\text{C}_{15}\text{H}_{32}$); 25—2-Tetradecanone ($\text{C}_{14}\text{H}_{28}\text{O}$); 26—Diethyl Phthalate ($\text{C}_{12}\text{H}_{14}\text{O}_4$); 27—2-Pentadecanone ($\text{C}_{15}\text{H}_{30}\text{O}$); 28—2-Hexadecanone ($\text{C}_{16}\text{H}_{32}\text{O}$); 29— γ -Tetradecalactone ($\text{C}_{14}\text{H}_{26}\text{O}_2$).

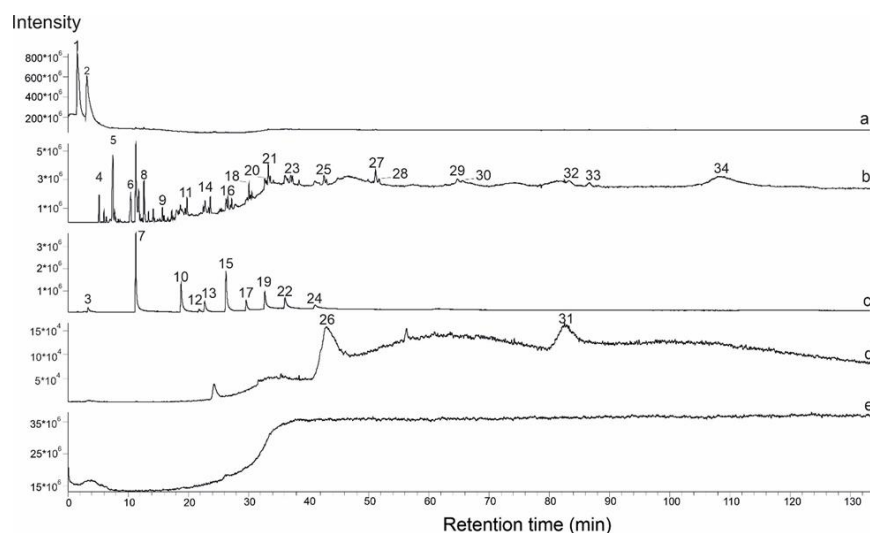


Figure 10. Results of GC–MS analysis of volatiles extracted via mechanical shock crushing from quartz D-1-2 of the Dobroe deposit. Total ion chromatogram (TIC) (a) and reconstructed ion chromatograms (RIC) for m/z (43 + 57 + 71 + 85) (b), m/z 60 (c), m/z 149 (d), and blank (TIC) (e). 1—Nitrogen (N_2); 2—water (H_2O); 3—Carbonyl sulfide (COS); 4—Acetaldehyde ($\text{C}_2\text{H}_4\text{O}$); 5—2-Propanone ($\text{C}_3\text{H}_6\text{O}$); 6—*n*-Butanal ($\text{C}_4\text{H}_8\text{O}$); 7—Acetic acid ($\text{C}_2\text{H}_4\text{O}_2$); 8—1-Butanol ($\text{C}_4\text{H}_{10}\text{O}$); 9—*n*-Heptane (C_7H_{16}); 10—*n*-Butanoic acid ($\text{C}_4\text{H}_8\text{O}_2$); 11—*n*-Octane (C_8H_{18}); 12—3-Methylbutanoic acid ($\text{C}_5\text{H}_{10}\text{O}_2$); 13—*n*-Pentanoic acid ($\text{C}_5\text{H}_{10}\text{O}_2$); 14—*n*-Nonane (C_9H_{20}); 15—*n*-Hexanoic acid ($\text{C}_6\text{H}_{12}\text{O}_2$); 16—*n*-Octanal ($\text{C}_8\text{H}_{16}\text{O}$); 17—*n*-Heptanoic acid ($\text{C}_7\text{H}_{14}\text{O}_2$); 18—*n*-Nonanal ($\text{C}_9\text{H}_{18}\text{O}$); 19—*n*-Octanoic acid ($\text{C}_8\text{H}_{16}\text{O}_2$);

20—2-Decanone (C₁₀H₂₀O); 21—n-Decanal (C₁₀H₂₀O); 22—n-Nonanoic acid (C₉H₁₈O₂); 23—1-Tridecene (C₁₃H₂₆); 24—n-Decanoic acid (C₁₀H₂₀O₂); 25—1-Tetradecene (C₁₄H₂₈); 26—Methyl 3-methoxy-4-methylbenzoate (C₁₀H₁₂O₃); 27—1-Pentadecene (C₁₅H₃₀); 28—Pentadecane (C₁₅H₃₂); 29—Tetradecanal (C₁₄H₂₈O); 30—n-Hexadecane (C₁₆H₃₄); 31—Diethyl Phthalate (C₁₂H₁₄O₄); 32—1-Heptadecene (C₁₇H₃₄); 33—n-Heptadecane (C₁₇H₃₆); 34—2-Methylheptadecane (C₁₈H₃₈).

4.4. Carbon Isotopic Composition ($\delta^{13}\text{C}$) of Carbon Dioxide in Fluid Inclusions

Carbon isotopes ($\delta^{13}\text{C}$) of carbonic acid were measured for fluid inclusions in quartz from the gold-bearing (n = 8) and barren (n = 3) zones (Table 4, Figure 11). The values of $\delta^{13}\text{C}_{\text{CO}_2}$ in fluids of the gold-bearing zone varied from -4.9 to -8.3‰ , showing a rather narrow range of fluctuations. A lighter carbon isotope ($\delta^{13}\text{C}_{\text{CO}_2} = -11.3\text{‰}$) was determined in the fluids of the barren zone, and the range of values expanded to a range of -3.6 to -11.3‰ (Figure 5).

Table 4. Carbon isotope composition ($\delta^{13}\text{C}$) of carbon dioxide in fluid inclusions in quartz from the Dobroe gold deposit.

Sample No.	$\delta^{13}\text{C}_{\text{CO}_2}$, ‰ (VPDB)
Gold-bearing zone	
D-1	-6.7
D-2	-7.2
D-4	-6.4
D-10	-4.9
D-2-3	-8.3
D-2-12	-7.4
D-2-13	-7.7
D-2-17	-7.1
Barren zone	
D-1-2	-7.5
D-1-3	-11.3
D-1-17	-3.6

Note: The carbon isotopic compositions ($\delta^{13}\text{C}$) of carbon dioxide in fluid inclusions were determined at the Analytical Center for Multi-Elemental and Isotope Research SB RAS, Novosibirsk. Analysts: V.N. Reutsky, M.N. Kolbasova, O.P. Izokh.

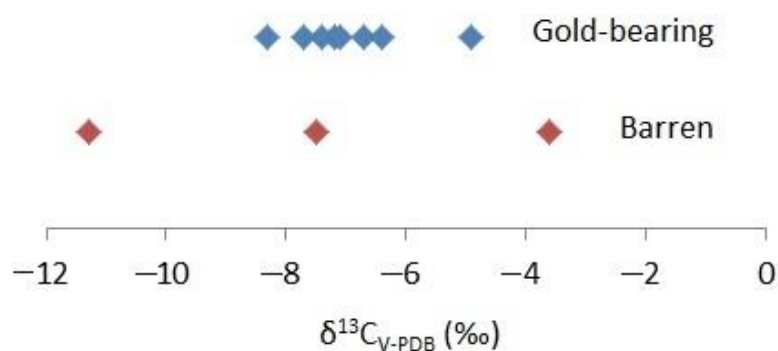


Figure 11. Isotope composition of the carbon ($\delta^{13}\text{C}$) of carbon dioxide from fluid inclusions in quartz of the Dobroe deposit: gold-bearing and barren zones.

4.5. Sulfur Isotopic Composition of Sulfides

Sulfur isotopes ($\delta^{34}\text{S}$) were measured in 10 sulfide monofractions, including arsenopyrite-3, pyrite-4, and pyrrhotite-3 (Table 5, Figure 12). In arsenopyrite, the $\delta^{34}\text{S}$ values had a rather narrow range of 1.9 to 4.2‰, and the same narrow range was present in pyrrhotite, whose values ranged from 6.0 to 9.0‰. In pyrite, the $\delta^{34}\text{S}$ fluctuated within a wider range from 3.2 to 17.0‰ (Figure 12).

Table 5. Sulfur isotopic composition of sulfides from the Dobroe gold deposit.

Sample No.	Mineral	$\delta^{34}\text{S}$, ‰
Gold-bearing zone		
D-10	Arsenopyrite	1.9
D-4	Arsenopyrite	3.8
D-2-12	Arsenopyrite	4.2
D-2	Pyrrhotite	6.0
D-2-13	Pyrrhotite	9.0
D-1	Pyrite	3.2
Barren zone		
D-1-2	Pyrite	10.5
D-1-17	Pyrite	15.2
D-1-12	Pyrite	17.0
D-1-3	Pyrrhotite	8.8

Note: The sulfur isotopic composition of sulfides was determined at the Analytical Center for Multi-Elemental and Isotope Research SB RAS, Novosibirsk. Analysts: V.N. Reutsky, M.N. Kolbasov.

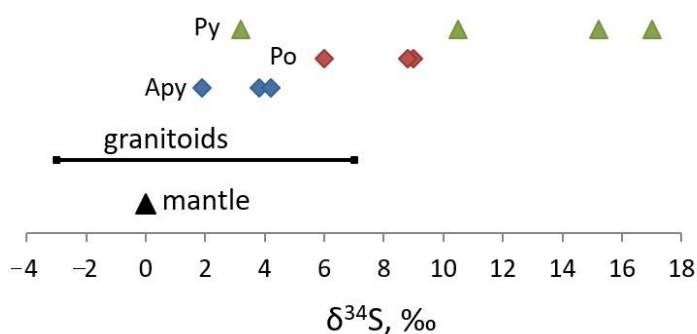


Figure 12. Variations in the sulfur isotopic composition of sulfides from the Dobroe deposit: Apy—arsenopyrite, Po—pyrrhotite, Py—pyrite. The sulfur isotopic composition of sulfides from granitoids is given according to [51].

5. Discussion

The data obtained in this study of fluid inclusions in the quartz and sulfides of the Dobroe gold deposit allow us to conclude that two types of fluid took part simultaneously or sequentially in the formation of the deposit: water–carbon dioxide, and carbon dioxide–hydrocarbon. The water–carbon dioxide type of fluid is indicated by the data obtained via Raman spectroscopy of individual vapor–liquid inclusions (type A) in quartz containing a water phase and a CO₂-dominated vapor phase (Table 2, Figure 3). This is also indicated by the GC–MS data (Table 3, Figure 4). The fluid consistently contains CO₂ and H₂O in various proportions. The carbon dioxide–hydrocarbon composition of the fluid present in the inclusions (type B) is also confirmed by the data obtained via both Raman spectroscopy (Table 2, Figure 3) and GC–MS (Table 3, Figure 4). These distinguished types of fluid differ in redox properties. The carbon dioxide–hydrocarbon type of fluid is more reduced than the water–carbon dioxide type, as evidenced by the CO₂/CH₄ ratio. According to a number of researchers [17,52–58], the /CH₄ ratio of a fluid is an indicator of hydrothermal system redox conditions.

According to the Raman spectroscopy analysis, in water–carbon dioxide (type A) inclusions, the CO₂/CH₄ ratio ranges from 1.7 to 329.3 (Table 2), averaging 31.0 (n = 28). In the carbon dioxide–hydrocarbon (type B) inclusions, the CO₂/CH₄ value varies from 0.04 to 30.5, averaging 4.2 (n = 18) (Table 2, Figure 3). From this, it follows that in the process of ore deposition, the redox properties of the fluids changed. This is also indicated by the data on the gross composition of volatiles obtained via GC–MS (Table 3). The H/(H + O) ratio calculated using the GC–MS data was 0.44–0.65. Alkanes/alkenes ratios were also used to reconstruct the redox potential of fluids, as suggested in [59,60]. According to Table 3, in

the arsenopyrite of the Dobroe deposit, co-crystallizing with gold, the value of the ratio of alkanes/alkenes was on average 28.3 ($n = 3$), and in quartz it was 7.5 ($n = 8$). Therefore, we can infer that the fluids transporting ore elements were reduced.

The fluids that formed the Dobroe gold deposit are represented by complex chemical compounds. Up to 200 chemical compounds were found in the compositions of the fluids (Table 3). The main components included CO_2 , H_2O , N_2 , and a large group of hydrocarbon compounds. The proportion of hydrocarbons in the fluids of the Dobroe deposit was up to seven times lower than in the fluids of the native gold of the Sovetskoe deposit [36], and up to eleven times lower than in the fluids of the gold-bearing acicular arsenopyrite of the Olimpiada deposit [22]. Consequently, the gold potential of mineralization may depend on the amount of reduced carbon dioxide–hydrocarbon compounds in the ore-forming fluid. This is reflected in the saturation degree of quartz and sulfides with inclusions filled with reduced carbon dioxide–hydrocarbon fluid. Another difference between the fluids of the large (>100 t Au) Sovetskoe, Blagodatnoe, and Olimpiada deposits and the small (<10 t) Dobroe deposit has been revealed. The gold-bearing fluids of large deposits were found to contain a reduced amount of water: <0.3 rel.% in native gold of the Sovetskoe deposit [36], 7.3 rel.% in native gold of the Blagodatnoe deposit [61], and <13.7 rel.% in gold-bearing acicular arsenopyrite from the Olimpiada deposit [22]. Meanwhile, in the fluids of arsenopyrite from the Dobroe deposit, the water content reaches 74.5 rel.% (Figure 13). Water-depleted mineral-forming fluids of the large Perron gold deposit (Abitibi Belt, Canada) were reported by [62]. The authors concluded that gold was not transported by water complexes, but was transported mainly by CO_2 and hydrocarbons, forming organometallic complexes with them. The same results were obtained by us when studying the fluids of a number of gold deposits of the Yenisei Ridge [14,20–22,25,36].

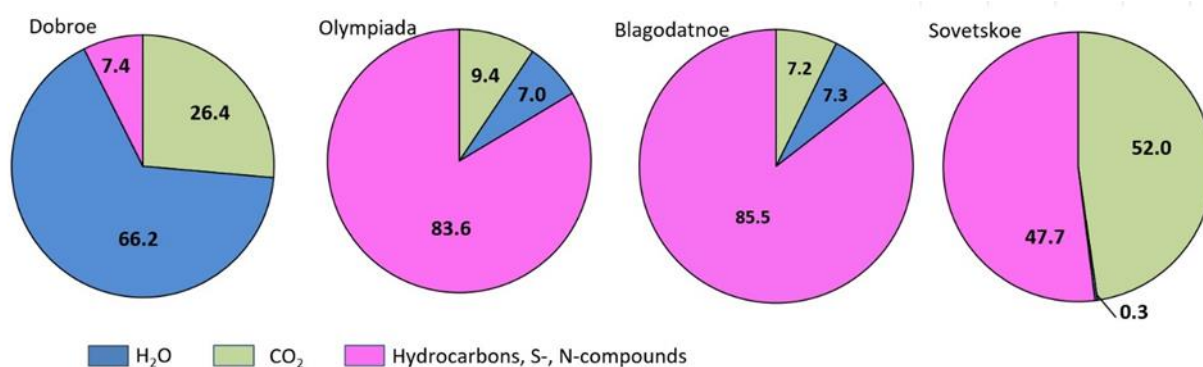


Figure 13. Content (rel.%) of hydrocarbons, carbon dioxide, and water in fluids from the Dobroe (arsenopyrite, sample D–2–12), Olimpiada (arsenopyrite, sample 503–39) [22], Blagodatnoe (native gold, sample 310–13) [61], and Sovetskoe (native gold, sample 375) [36].

Another unique feature of fluids from the Dobroe deposit is that quartz fluids contain high (up to 47 rel.%) contents of nitrogenated compounds (Table 3), among which the proportion of molecular nitrogen (N_2) makes up more than 90%. An abundance of N_2 (up to 90 mol.%) was also noted in the gas phase of individual fluid inclusions via Raman spectroscopy (Table 2). Elevated concentrations of molecular nitrogen in fluids were determined in quartz taken from quartz veins which were 2–5 cm thick hosted by the carbonaceous schist of the Dobroe deposit. The selvages of these veins also contained carbonaceous schists, while the vein itself contained xenoliths of carbonaceous schists.

According to [63], molecular nitrogen is a chemically inactive substance. Its inertness is due to the greater strength within the molecular bond, the breaking of which requires high energy. However, chemical compounds containing nitrogen in the form of the CN–ligand can enter into complex formation reactions with gold and transport it to the deposit sites [64]. The appearance of N_2 in the fluid in considerable amounts may be associated with chemical reactions between heated fluids and the ammonium-bearing silicates of

ore-bearing rocks [30,65,66]. The presence of N_2 in the fluid may also be associated with the organic matter decomposition of the carbonaceous schists present in the field. Decomposition proceeds most intensively in zones of maximal hydrothermal–metasomatic development of host rocks, where the role of ammonium nitrogen decreases and N_2 becomes the predominant component [67,68]. A point of view has been expressed regarding the supply of N_2 during degassing from the deep zones of the Earth's crust and even, in some cases, from the mantle [69,70].

Hydrothermal activity at the Dobroe deposit began with the formation of early quartz veins, veinlets, and lenses involving the metamorphogenic rearrangement of silica in host rocks. In subsequent geological periods, in zones of tectonic disturbance, early quartz formations underwent a local pressure gradient. This resulted in the rearrangement (granulation) of quartz. In these places, quartz acquired a granoblastic structural pattern (Figure 2). Then, vein quartz (Quartz 2) crystallized as large grains and veinlets, intersecting granoblastic quartz (Quartz 1) (Figure 2) with the new portion of fluid inflow at a temperature of 300–360 °C. In the grains of granoblastic quartz, many mutually intersecting microcracks appeared, filling mainly with gaseous secondary inclusions (Figure 4c).

The Dobroe deposit was formed by water—carbon dioxide—hydrocarbon fluids in the temperature range of 180 to 360 °C, with pressure ranging from 0.8 to 1.3 kbar and salinity from 1.5 to 15.0 wt.%, NaCl-equiv. (Table 1, Figure 14). Wide variations in temperature, pressure, and salinity are characteristic of many gold deposits on the Yenisei Ridge [19–23,25–27]. They reflect the complex and lengthy process of the ore formation.

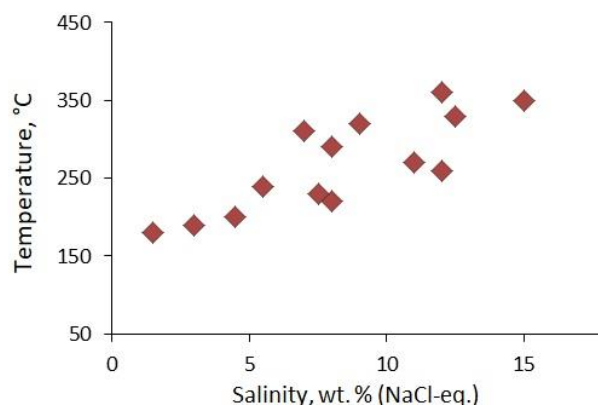


Figure 14. Temperature and salinity variations during quartz vein zones formation at the Dobroe deposit (primary and pseudosecondary FI data).

The thermobarogeochemical characteristics (T, P, composition) of fluids trapped by primary inclusions in Quartz 2 and secondary inclusions in Quartz 1 are similar (Tables 1–3) (Figure 4). This indicates successive crystallization of first granoblastic and then veined quartz. Moreover, this points to the high penetrating ability of gaseous carbon dioxide–hydrocarbon fluids, which move through numerous microcracks in granoblastic quartz.

Carbon isotopic studies ($\delta^{13}C$) of carbon dioxide in fluid inclusions from gold-bearing and barren quartz of the Dobroe deposit showed close values ranging from -3.6 to -11.3 ‰ (Table 4, Figure 11). Carbons with such values are much heavier than organic carbon of terrigenous layers, for which $\delta^{13}C$ ranges from -22.4 to -28.7 ‰ [71–74]. The increase in $\delta^{13}C_{CO_2}$ in the quartz fluids of the Dobroe deposit could be caused by the influx of CH_4 into the fluid system in the temperature range of 250–350 °C [51]. The Dobroe deposit was formed at these same temperatures (Table 1), and the fluids consistently contain CH_4 and other hydrocarbons and their derivatives which are heavier than methane (Tables 2 and 3). The most plausible source of $\delta^{13}C$ found in the fluid of the Dobroe deposit is intracrustal fluids.

The isotopic composition of sulfur was determined in arsenopyrite, pyrrhotite, and pyrite (Table 5, Figure 12). The $\delta^{34}S$ values of arsenopyrite and pyrrhotite are found

to remain within rather narrow ranges, from +1.9 to +4.2‰ and from +6.0 to +9.0‰, respectively. The range of $\delta^{34}\text{S}$ variations in pyrite significantly expands—from +3.2 to +17‰. The wide range of sulfur isotope values in pyrite can be explained by variations in redox conditions, as confirmed by the results of the Raman spectroscopy and the GC-MS. On the basis of isotopic data, sulfur in the sulfides of the deposit (from +1.9 to +17‰) can be obtained by “averaging” the sulfur of host rocks, and these values indicate a crustal nature [18,51]. At the same time, as $\delta^{34}\text{S}$ values approach the “mantle” level, sulfur in the sulfides of the Dobroe deposit could be partially brought forth by fluids of a deeper nature.

6. Conclusions

The Dobroe gold deposit, with probable gold reserves of less than 10 tonnes, was formed by oxidized water–carbon dioxide and reduced carbon dioxide–hydrocarbon fluids in temperatures ranging from 180 to 360 °C, pressures ranging from 0.8 to 1.3 kbar, and salinities ranging from 1.5 to 15.0 wt.%, NaCl-equiv.

Ore-forming fluids consist of H_2O ; CO_2 ; N-, S-, and Cl-compounds; and hydrocarbons, which are potentially capable of transporting ore elements.

The gold contents of quartz-vein formations increase when reduced gaseous carbon dioxide–hydrocarbon fluids are superimposed on early barren parageneses.

The elevated hydrocarbon content of the ore-forming fluid may indicate the gold potential of quartz-vein zones. Presumably, the fluid supply occurred due to the sedimentary rocks’ devolatilization during the tectonic activation of the Yenisei Ridge. Further, the fluid formed metalliferous quartz veins in the fault zones.

Supplementary Materials: The following supporting information can be downloaded at: <https://www.mdpi.com/article/10.3390/min13010011/s1>. Table S1: Results of GC–MS analysis of volatiles extracted via mechanical shock destruction from vein quartz (Dobroe deposit, Yenisei ridge). 161 components. Table S2: Results of GC–MS analysis of volatiles extracted via mechanical shock destruction from granoblastic quartz (Dobroe deposit, Yenisei ridge). 162 components. Table S3: Results of GC–MS analysis of volatiles extracted via mechanical shock destruction from vein quartz (Dobroe, Yenisei ridge). 135 components. Table S4: Results of GC–MS analysis of volatiles extracted via mechanical shock destruction from granoblastic quartz (Dobroe deposit, Yenisei ridge). 142 components. Table S5: Results of GC–MS analysis of volatiles extracted via mechanical shock destruction from granoblastic quartz (Dobroe deposit, Yenisei ridge). 149 components. Table S6: Results of GC–MS analysis of volatiles extracted via mechanical shock destruction from vein quartz (Dobroe deposit, Yenisei ridge). 127 components. Table S7: Results of GC–MS analysis of volatiles extracted via mechanical shock destruction from arsenopyrite (Dobroe deposit, Yenisei ridge). 148 components. Table S8: Results of GC–MS analysis of volatiles extracted via mechanical shock destruction from pyrite (Dobroe deposit, Yenisei ridge). 133 components. Table S9: Results of GC–MS analysis of volatiles extracted via mechanical shock destruction from arsenopyrite (Dobroe deposit, Yenisei ridge). 140 components. Table S10: Results of GC–MS analysis of volatiles extracted via mechanical shock destruction from arsenopyrite (Dobroe deposit, Yenisei ridge). 133 components. Table S11: Results of GC–MS analysis of volatiles extracted via mechanical shock destruction from granoblastic quartz (Dobroe deposit, Yenisei ridge). 188 components. Table S12: Results of GC–MS analysis of volatiles extracted via mechanical shock destruction from vein quartz (Dobroe deposit, Yenisei ridge). 201 components.

Author Contributions: Conceptualization, E.S., N.G. and A.T.; methodology, A.T. and T.B.; investigation, N.G., E.S., M.K., M.R. and M.P.; resources, A.S. and S.S.; writing—original draft preparation, E.S. and N.G.; writing—review and editing, A.T., T.B., A.S. and S.S. All authors have read and agreed to the published version of the manuscript.

Funding: This work was supported by Ministry of Science and Higher Education of the Russian Federation (grant No. 13.1902.21.008, agreement 075–15–2020–802).

Data Availability Statement: Data are contained within the article or Supplementary Material.

Conflicts of Interest: The authors declare no conflict of interest.

References

1. Borisenko, A.S.; Sazonov, A.M.; Nevolko, P.A.; Naumov, E.A.; Tessalina, S.; Kovalev, K.R.; Sukhorukov, V.P. Gold Deposits of the Yenisei Ridge (Russia) and Age of Its Formation. *Acta Geol. Sin.* **2014**, *88* (Suppl. 2), 686–687. [[CrossRef](#)] [[PubMed](#)]
2. Goryachev, N.A. Gold deposits in the Earth's history. *Geol. Ore Depos.* **2019**, *61*, 495–511. [[CrossRef](#)]
3. Serdyuk, S.S.; Zabayaka, A.I.; Gusarov, Y.V. Gold. In *Tectonics and Metallogeny of Lower Angara Region*; KNIIGiMS: Krasnoyarsk, Russia, 2004; pp. 203–221. (In Russian)
4. Serdyuk, S.S.; Komorovsky, Y.E.; Zverev, A.I.; Oyaber, V.K.; Vlasov, V.S.; Babushkin, V.E.; Kirillenko, V.A.; Zemlyansky, S. *Models of Gold Deposits in Yenisei Siberia, Krasnoyarsk*; Siberian Federal University: Krasnoyarsk, Russia, 2010; 584p. (In Russian)
5. Poleva, T.V.; Sazonov, A.M. *Geology of the Blagodatnoye Gold Deposit in the Yenisei Ridge*; ITKOR: Moscow, Russia, 2012; p. 292. (In Russian)
6. Sazonov, A.M.; Zvyagina, E.A.; Silyanov, S.A.; Lobanov, K.V.; Leontiev, S.I.; Kalinin, Y.A.; Savichev, A.A.; Tishin, P.A. Ore genesis of the Olimpiada gold deposit (Yenisei Ridge, Russia). *Geospheric Res.* **2019**, *1*, 17–43. [[CrossRef](#)]
7. Sazonov, A.M.; Ananyev, A.A.; Poleva, T.V.; Khokhlov, A.N.; Vlasov, V.S.; Zvyagina, E.A.; Fedorova, A.V.; Tishin, P.A.; Leontiev, S.I. Gold ore metallogeny of the Yenisei ridge: Geological-structural position, structural types of ore fields. *Tekhnika I Tekhnologii Zh. Sib. Federal. Univ.* **2010**, *4*, 371–395.
8. Polyakov, A.V. Assessment of efficiency of development of the group of gold deposits by the example of Razdolinsky ore cluster. In *State and Problems of Geological Study of Subsoil and Development of Mineral and Raw Material Base of Krasnoyarsk Region*; KNIIGiMS: Krasnoyarsk, Russia, 2003; pp. 239–241. (In Russian)
9. Silyanov, S.A.; Sazonov, A.M.; Tishin, P.A.; Nekrasova, N.A.; Lobastov, B.M.; Zvyagina, E.A.; Ryabukha, M.A. Geochemical indicators of the genesis of the Panimba gold deposit at the Yenisei Ridge (Siberia, Russia). *Geospheric Res.* **2018**, *3*, 6–21. (In Russian) [[CrossRef](#)]
10. Groves, D.I.; Goldfarb, R.J.; Santosh, M. The conjunction of factors that lead to formation of giant gold provinces and deposits in non-arc settings. *Geosci. Front.* **2016**, *7*, 303–314. [[CrossRef](#)]
11. Petrov, V.G. *Gold Conditions in the Northern Part of the Yenisei Ridge*; Nauka: Novosibirsk, Russia, 1974; 96p. (In Russian)
12. Buryak, V.A. *Metamorphism and Ore Formation*; Nedra: Moscow, Russia, 1982; 256p. (In Russian)
13. Novozhilov, Y.I.; Gavrilov, A.M. *Gold-Sulfide Deposits in Carbon-Terrigenous Strata*; TsNIGRI: Moscow, Russia, 1999; 175p. (In Russian)
14. Tomilenko, A.A.; Gibsher, N.A. Composition of Fluids in Mineralized and Barren Zones of the Sovetskoe Quartz-Gold Deposit, Yenisei Ridge as Deduced from Fluid Inclusions Study. *Geochem. Int.* **2001**, *39*, 167–177.
15. Li, L.V. *Olimpiadinskoe Deposit of Disseminated Gold-Sulfide Ores*; KNIIGiMS: Krasnoyarsk, Russia, 2003; 120p. (In Russian)
16. Kryazhev, S.G.; Grinenko, V.A. The isotopic composition and sources of sulfur in gold-sulphide deposits of the Yenisei Ridge. In *Abstracts of the XVIII Symposium on Geochemistry of Isotopes*; GEOKhI RAN: Moscow, Russia, 2007; p. 37. (In Russian)
17. Kryazhev, S.G. Modern problems of the theory and practice of thermobarogeochemistry. *Rudy Met.* **2010**, *2*, 38–46. (In Russian)
18. Kryazhev, S.G. Genetic Models and Criteria for Prediction of Gold Deposits in Carbon-Terrigenous Complexes. Ph.D. Thesis, TsNIGRI, Moscow, Russia, 2017. (In Russian).
19. Tomilenko, A.A.; Gibsher, N.A.; Dublaynsky, Y.V.; Dallai, I. Geochemical and isotopic properties of fluid from gold-bearing and barren quartz veins of the Sovetskoye deposit (Siberia, Russia). *Econ. Geol.* **2010**, *105*, 375–394. [[CrossRef](#)]
20. Gibsher, N.A.; Tomilenko, A.A.; Sazonov, A.M.; Ryabukha, M.A.; Timkina, A.L. The Gerfed gold deposit: Fluids and PT-conditions for quartz vein formation (Yenisei Ridge, Russia). *Russ. Geol. Geophys.* **2011**, *52*, 1461–1473. [[CrossRef](#)]
21. Gibsher, N.A.; Ruabukha, M.A.; Tomilenko, A.A.; Sazonov, A.M.; Khomenko, M.O.; Bul'bak, T.A.; Nekrasova, N.A. Metal-bearing fluids and the age of the Panimba gold deposits (Yenisei Ridge, Russia). *Russ. Geol. Geophys.* **2017**, *58*, 1366–1383. [[CrossRef](#)]
22. Gibsher, N.A.; Tomilenko, A.A.; Bul'bak, T.A.; Ryabukha, M.A.; Khomenko, M.O.; Shaparenko, E.O.; Sazonov, A.V.; Sil'yanov, S.A.; Nekrasova, N.A. The Olimpiadinskoe gold deposit (Yenisei ridge): Temperature, pressure, composition of ore-forming fluids, $\delta^{34}\text{S}$ in sulfides, $3\text{He}/4\text{He}$ of fluids, Ar–Ar age, and duration of formation. *Russ. Geol. Geophys.* **2019**, *60*, 1043–1059. [[CrossRef](#)]
23. Gibsher, N.A.; Sazonov, A.M.; Travin, A.V.; Tomilenko, A.A.; Ponomarchuk, A.V.; Sil'yanov, S.A.; Nekrasova, N.A.; Shaparenko, E.O.; Ryabukha, M.A.; Khomenko, M.O. Age and Duration of the Formation of the Olimpiada Gold Deposit (Yenisei Ridge, Russia). *Geochem. Int.* **2019**, *57*, 593–599. [[CrossRef](#)]
24. Novozhilov, Y.; Gavrilov, A.M.; Yablokova, S.V.; Aref'eva, V.A. Unique economic Olimpiada gold-sulfide deposits in the Upper Proterozoic terrigenous sediments. *Rudy Met.* **2014**, *3*, 51–64.
25. Ryabukha, M.A.; Gibsher, N.A.; Tomilenko, A.A.; Bul'bak, T.A.; Khomenko, M.O.; Sazonov, A.M. PTX—Parameters of metamorphic and hydrothermal fluids; isotopy and age of formation of the Bogunai gold deposit, southern Yenisei ridge (Russia). *Russ. Geol. Geophys.* **2015**, *56*, 1153–1172. [[CrossRef](#)]
26. Shaparenko, E.; Gibsher, N.; Tomilenko, A.; Sazonov, A.; Bul'bak, T.; Ryabukha, M.; Khomenko, M.; Silyanov, S.; Nekrasova, N.; Petrova, M. Ore-Bearing Fluids of the Blagodatnoye Gold Deposit (Yenisei Ridge, Russia): Results of Fluid Inclusion and Isotopic Analyses. *Minerals* **2021**, *11*, 1090. [[CrossRef](#)]
27. Prokof'ev, V.Y.; Afanasyeva, Z.B.; Ivanova, G.F.; Boiron, M.K.; Marignyak, H. Study of fluid inclusions in minerals of the Olimpiada Au–(Sb–W) deposit (Yenisei ridge) (In Russian). *Geochemistry* **1994**, *7*, 1012–1029.
28. Afanas'eva, Z.B.; Ivanova, G.F.; Miklishanskiy, A.Z.; Romashova, T.V.; Kolesov, G.M. Geochemical characteristics of tungsten mineralization of the Olimpiada gold-sulfide deposit (Yenisei ridge). *Geochemistry* **1995**, *1*, 29–47. (In Russian)

29. Baranova, N.N.; Afanas'eva, Z.B.; Ivanova, G.F.; Mironova, O.F.; Kolpakova, N.N. Character of ore-forming processes at the Olimpiada Au (Sb, W) deposit (based on the study of mineral paragenesis and fluid inclusions). *Geochemistry* **1997**, *3*, 282–293. (In Russian)
30. Genkin, A.D.; Wagner, F.E.; Krylova, T.L.; Tsepina, A.I. Gold-bearing arsenopyrite and its formation condition at the Olimpiada and Veduga gold deposits (Yenisei ridge, Siberia) (In Russian). *Geol. Ore Depos.* **2002**, *44*, 59–76.
31. Gertner, I.; Tishin, P.; Vrublevskii, V.; Sazonov, A.; Zvyagina, E.; Kolmakov, Y. Neoproterozoic alkaline igneous rocks, carbonatites and gold deposits of the Yenisei ridge, Central Siberia: Evidence of mantle plume activity and late collision shear tectonics associated with orogenic gold mineralization. *Resour. Geol.* **2011**, *61*, 316–343. [[CrossRef](#)]
32. Vernikovskiy, V.A.; Vernikovskaya, A.E. Tectonics and evolution of granitoid magmatism in the Yenisei Ridge. *Russ. Geol. Geophys.* **2006**, *47*, 32–50.
33. Goldfarb, R.J.; Groves, D.I. Orogenic gold: Common vs. evolving fluid and metal sources through time. *Lithos* **2015**, *223*, 2–26. [[CrossRef](#)]
34. Groves, D.I.; Santosh, M.; Deng, J.; Wang, Q.; Yang, L.; Zhang, L. A holistic model for the origin of orogenic gold deposits and its implications for exploration. *Miner. Depos.* **2020**, *55*, 275–292. [[CrossRef](#)]
35. Groves, D.I.; Santosh, M.; Müller, D.; Zhang, L.; Deng, J.; Yang, L.-Q.; Wang, Q.-F. Mineral systems: Their advantages in terms of developing holistic genetic models and for target generation in global mineral exploration. *Geosystems Geoenvironment* **2022**, *1*, 100001. [[CrossRef](#)]
36. Bul'bak, T.A.; Tomilenko, A.A.; Gibsher, N.A.; Sazonov, A.M.; Shaparenko, E.O.; Ryabukha, M.A.; Khomenko, M.O.; Sil'yanov, S.A.; Nekrasova, N.A. Hydrocarbons in Fluid Inclusions from Native Gold, Pyrite, and Quartz of the Sovetskoe Deposit (Yenisei Ridge, Russia) According to Pyrolysis-Free Gas Chromatography-Mass Spectrometry Data. *Russ. Geol. Geophys.* **2020**, *61*, 1260–1282. [[CrossRef](#)]
37. Brovko, G.N.; Li, L.V.; Sherman, M.L. *Geology and Metallogeny of the Yenisei Ore Belt*; SNIIGGIMS; Ministerstvo Geologii SSSR: Krasnoyarsk, Russia, 1985; 289p. (In Russian)
38. Bernstein, P.S. Conditions of localization of different types of gold deposits of the Yenisei Ridge. *Proc. NIGRI Gold* **1951**, *18*, 26–31. (In Russian)
39. Bernstein, P.S.; Petrovskaya, N.V. *Sovetskoe Gold-Ore Deposit (Yenisei Ridge)*; Geology of the Major Gold-Ore Deposits of the USSR; Nauka: Moscow, Russia, 1954; Volume 6, 162p. (In Russian)
40. Brown, P.E.; Lamb, W.M. P-V-T properties of fluids in the system $H_2O \pm CO_2 \pm NaCl$: New graphical presentations and implications for fluid inclusion studies. *Geochim. Cosmochim. Acta* **1989**, *53*, 1209–1231. [[CrossRef](#)]
41. Duan, Z.; Moller, N.; Weare, J.H. A general equation of state for supercritical fluid mixtures and molecular dynamics simulation of mixture PVTX properties. *Geochim. Cosmochim. Acta* **1996**, *60*, 1209–1216. [[CrossRef](#)]
42. Bakker, R.J. Fluids: New software package to handle microthermometric data and to calculate isochors. *Memoir Geol. Soc.* **2001**, *7*, 23–25.
43. Steele-MacInnis, M.; Lecumberri-Sanchez, P.; Bodnar, R.J. HokieFlincs_ H_2O -NaCl: A Microsoft Excel spreadsheet for interpreting microthermometric data from fluid inclusions based on the PVTX properties of H_2O -NaCl. *Comput. Geosci.* **2012**, *49*, 334–337. [[CrossRef](#)]
44. Kirgintsev, A.N.; Trushnikova, L.I.; Lavrentieva, V.G. *Water Solubility of Inorganic Compounds*; A Handbook; Khimiya: Leningrad, Russia, 1972. (In Russian)
45. Borisenko, A.S. A Study of Salt Composition of Solutions Trapped in Vapor-Liquid Inclusions Using Cryometric Method. *Russ. Geol. Geophys.* **1977**, *8*, 16–27. (In Russian)
46. Dubessy, J.; Poty, B.; Ramboz, C. Advances in C-O-H-N-S fluid geochemistry based on micro-Raman spectrometric analysis of fluid inclusions. *Eur. J. Miner.* **1989**, *1*, 517–534. [[CrossRef](#)]
47. Burke, E.A.J. Raman microspectrometry of fluid inclusions. *Lithos* **2001**, *55*, 139–158. [[CrossRef](#)]
48. Frezzotti, M.L.; Tecce, F.; Casagli, A. Raman spectroscopy for fluid inclusion analysis. *J. Geochem. Exp.* **2012**, *112*, 1–20. [[CrossRef](#)]
49. Tomilenko, A.; Sonin, V.; Bul'bak, T.; Chepurov, A. Composition of volatile components in the polycrystalline CVD diamond (by coupled gas chromatographic-mass spectrometric analysis). *Carbon Lett.* **2019**, *29*, 327–336. [[CrossRef](#)]
50. Pal'yanova, G.A.; Reutsky, V.N.; Sobolev, E.S.; Bortnikov, N.S. Upper Triassic pyritized bivalve mollusks from the Sentachan orogenic gold-antimony deposit, Eastern Yakutia: Mineralogy and sulfur isotopic composition. *Geol. Ore Depos.* **2016**, *58*, 513–521. [[CrossRef](#)]
51. Ohmoto, H.; Rye, R.O. Isotopes of Sulfur and Carbon. In *Geochemistry of Hydrothermal Ore Deposits*; Wiley: New York, NY, USA, 1979; pp. 509–567.
52. Bortnikov, N.S.; Prokof'ev, V.Y.; Razdolina, N.V. Origin of the Charmitan gold-quartz deposit (Uzbekistan). *Geol. Ore Depos.* **1996**, *38*, 208–226. (In Russian)
53. Eirish, L.V. *Metallogeny of Gold of Priamurye (Amur region, Russia)*; Dalnauka: Vladivostok, Russia, 2002; 194p. (In Russian)
54. Kryazhev, S.G. *Isotope-Geochemical Regime of the Formation of the Gold Ore Deposit Muruntau*; TsNIGRI: Moscow, Russia, 2002. (In Russian)
55. Safonov, Y.G.; Prokof'ev, V.Y. Model of cosedimentation hydrothermal formation of gold-bearing reefs of the Witwatersrand basin. *Geol. Ore Depos.* **2006**, *48*, 475–511. [[CrossRef](#)]

56. Robert, F.; Kelly, W.C. Ore-forming fluids in Archean gold-bearing quartz veins at the Sigma Mine, Abitibi greenstone belt, Quebec, Canada. *Econ. Geol.* **1987**, *82*, 1464–1482. [[CrossRef](#)]
57. Jia, Y.; Li, X.; Kerrich, R. A Fluid Inclusion Study of Au-Bearing Quartz Vein Systems in the Central and North Deborah Deposits of the Bendigo Gold Field, Central Victoria, Australia. *Econ. Geol.* **2000**, *95*, 467–494. [[CrossRef](#)]
58. Ronde, C.E.J.; Faure, K.; Bray, C.J.; Whitford, D.J. Round Hill shear zone-hosted gold deposit, Macraes Flat, Otago, New Zealand; evidence of a magmatic ore fluid. *Econ. Geol.* **2000**, *95*, 1025–1048. [[CrossRef](#)]
59. Norman, D.I.; Blamey, N.; Moore, J.N. Interpreting geothermal processes and fluid sources from fluid inclusion organic compounds and CO₂/N₂ ratios. In Proceedings of the 27th Workshop on Geothermal Reservoir Engineering, Stanford, CA, USA, 28–30 January 2002; pp. 234–241.
60. Blamey, N.J.F. Composition and evolution of crustal geothermal and hydrothermal fluids interpreted using quantitative fluid inclusion gas analysis. *J. Geochem. Exp.* **2012**, *116–117*, 17–27. [[CrossRef](#)]
61. Shaparenko, E.O. Physico-Chemical Conditions of the Blagodantnoye and Dobroe Gold Deposits Formation (Yenisei Ridge). Ph.D. Thesis, V.S. Sobolev Institute of Geology and Mineralogy SB RAS, Novosibirsk, Russia, 2022. (In Russian).
62. Gaboury, D.; Genna, D.; Trottier, J.; Bouchard, M.; Augustin, J.; Malcolm, K. The Perron Gold Deposit, Archean Abitibi Belt, Canada: Exceptionally High-Grade Mineralization Related to Higher Gold-Carrying Capacity of Hydrocarbon-Rich Fluids. *Minerals* **2021**, *11*, 1066. [[CrossRef](#)]
63. Puddephatt, R.J. *The Chemistry of Gold*; Elsevier: Amsterdam, The Netherlands, 1980; 274p.
64. Marchuk, M.V. Transport of Major Elements and Metals in Reduced Fluids: An Experimental Study. Author's Abstract. Ph.D. Thesis, Institute of the Earth's Crust SB RAS, Irkutsk, Russia, 2008. (In Russian).
65. Mironova, O.F.; Naumov, V.B.; Salazkin, A.N. Nitrogen in Mineral-Forming Fluids. Gas Chromatography Determination on Fluid Inclusions in Minerals. *Geochem. Int.* **1992**, *7*, 979–991.
66. Bottrell, S.H.; Miller, M.F. The geochemical behaviour of nitrogen compounds during the formation of black shale hosted quartz-vein gold deposits, North Wales. *Appl. Geochem.* **1990**, *5*, 289–296. [[CrossRef](#)]
67. Kol'tsov, A.B. Hydrothermal mineralization in the fields of temperature and pressure gradients. *Geochem. Int.* **2010**, *11*, 1097–1111. [[CrossRef](#)]
68. Zubkov, V.S. Composition and speciation of fluids in the system C–H–N–O–S at P–T conditions of the upper mantle. *Geochem. Int.* **2001**, *39*, 131–145.
69. Sorokhtin, O.G.; Ushakov, S.A. *Evolution of Earth*; Moscow State University: Moscow, Russia, 2002; 560p.
70. Prokofiev, V.Y.; Naumov, V.B.; Mironova, O.F. Physicochemical parameters and geochemical features of fluids of Precambrian gold deposits. *Geochem. Int.* **2017**, *55*, 1047–1065. (In Russian) [[CrossRef](#)]
71. Galimov, E.M. *Geochemistry of Stable Carbon Isotopes*; Nedra: Moscow, Russia, 1968; 300p. (In Russian)
72. Hoefs, I. *Geochemistry of Stable Isotopes*; Mir: Moscow, Russia, 1983; 200p. (In Russian)
73. Kuleshov, V.N. Isotopic Composition and Origin of Deep Carbonates. *Proc. GIN AS USSR* **1986**, *409*, 128. (In Russian)
74. Avgenko, O.V.; Alexandrov, N.A.; Khudalozhkin, O.V. Degree of reduction, genesis and volumes of metamorphogenic fluid. In *Geology, Geochemistry and Geophysics at the Turn of XX and XXI Centuries*; IZK: Irkutsk, Russia, 2002; pp. 146–147. (In Russian)

Disclaimer/Publisher's Note: The statements, opinions and data contained in all publications are solely those of the individual author(s) and contributor(s) and not of MDPI and/or the editor(s). MDPI and/or the editor(s) disclaim responsibility for any injury to people or property resulting from any ideas, methods, instructions or products referred to in the content.